Article

Unconventional hexagonal open Prussian blue analog structures

Jinwen Yin [1,2,17], Jing Wang [3,4,17], Mingzi Sun [5,17], Yajie Yang [6,17], Jia Lyu [7,17], Lei Wang[5], Xinglong Dong[8,9], Chenliang Ye[10], Haibo Bao[11], Jun Guo [1], Bo Chen[1], Xichen Zhou [1], Li Zhai [1], Zijian Li [1], Zhen He[1], Qinxin Luo[1], Xiang Meng[1,2], Yangbo Ma [1], Jingwen Zhou [1,2], Pengyi Lu[1,2], Yunhao Wang [1], Wenxin Niu[11], Zijian Zheng [5], Yu Han [8,12], Daliang Zhang[7], Shibo Xi[13], Ye Yuan [6] ✉, Bolong Huang [5] ✉, Peng Guo [3,14] ✉ & Zhanxi Fan [1,2,15,16] ✉

Prussian blue analogs (PBAs), as a classical kind of microporous materials, have attracted substantial interests considering their well-defined framework structures, unique physicochemical properties and low cost. However, PBAs typically adopt cubic structure that features small pore size and low specific surface area, which greatly limits their practical applications in various fields ranging from gas adsorption/separation to energy conversion/storage and biomedical treatments. Here we report the facile and general synthesis of unconventional hexagonal open PBA structures. The obtained hexagonal copper hexacyanocobaltate PBA prisms (H-CuCo) demonstrate large pore size and specific surface area of 12.32 Å and 1273 $m^2\,g^{-1}$, respectively, well exceeding those (5.48 Å and 443 $m^2\,g^{-1}$) of traditional cubic CuCo PBA cubes (C-CuCo). Significantly, H-CuCo exhibits much superior gas uptake capacity over C-CuCo toward carbon dioxide and small hydrocarbon molecules. Mechanism studies reveal that unsaturated Cu sites with planar quadrilateral configurations in H-CuCo enhance the gas adsorption performance.

As a classical category of microporous materials, Prussian blue analogs (PBAs)[1–3] have shown promising applications in various important fields, including gas adsorption[4–12], catalysis[13–18], energy storage[19–24], photothermal therapy[25–27], drug delivery[26,28–30], sensing[31–33], and nanozyme[34,35]. In general, the theoretical formula of PBAs is M[M′(CN)$_6$], where M and M′ normally represent early transition metals (M = Cu, Co, Ni, Fe, Zn, etc.; M′ = Mn, Fe, Co) and the octahedral [M′(CN)$_6$]$^{n-}$ complexes are linked via octahedrally-coordinated nitrogen-bound M^{n+} ions, forming the conventional cubic structure ($Fm\bar{3}m$ space group)[3,36], such as Cu$_3$[Co(CN)$_6$]$_2$[11,37,38]. Unfortunately, the common cubic structure of PBAs typically features a small pore size and low specific surface area, usually around 4.5 Å and less than 900 $m^2\,g^{-1}$, respectively[7,8,11,12,39–42], which significantly limit their performances and broad applications such as gas storage.

In order to boost their performance for various applications, defect engineering of PBAs by creating either [M′(CN)$_6$][12,43–46] or CN defects[15,37,47,48] has been developed and widely applied to regulate their structures and properties. However, the distribution of defects in PBAs is usually random and aperiodic[8,20,31,49], which makes it difficult to study the crystal structure at the atomic scale and especially challenging to uncover the precise structure-performance relationship as well. Meanwhile, the existence of defects in PBAs also makes the structure unstable and prone to collapse[50,51]. Therefore, developing an alternative and feasible strategy to modulate the structure of PBAs is significant and highly essential to modulating the intrinsic properties of PBAs toward distinct practical scenarios.

Here we report a facile and general co-precipitation method for synthesizing hexagonal phase PBAs with high crystallinity and open structure, including hexagonal copper hexacyanocobaltate PBA

prisms (denoted as H-CuCo) and CuCo-based PBAs with hexagonal phase like $Fe_{0.1}$-CuCo, $Fe_{0.2}$-CuCo, $Co_{0.1}$-CuCo, $Ni_{0.1}$-CuCo and $Zn_{0.1}$-CuCo (the subscript numbers, i.e., 0.1 and 0.2, represent the feeding proportion of doping element with respect to Cu during the synthesis process). The structure of H-CuCo is systematically characterized by powder X-ray diffraction (PXRD), three-dimensional (3D) electron diffraction, spherical aberration-corrected high-resolution transmission electron microscope (C_s-HRTEM), selected-area electron diffraction (SAED), X-ray photoelectron spectroscopy (XPS) and X-ray absorption spectroscopy (XAS). H-CuCo possesses a large pore size of 12.32 Å and a high specific surface area of 1273 $m^2 g^{-1}$, well surpassing those (5.48 Å and 443 $m^2 g^{-1}$) of common cubic CuCo PBA cubes (denoted as C-CuCo), respectively. As a proof-of-concept application, the gas adsorption performance of H-CuCo is studied toward carbon dioxide (CO_2) and small hydrocarbon molecules, which also greatly outperforms that of C-CuCo. In particular, the CO_2 uptake capacity of H-CuCo reaches up to 6.1 mmol g^{-1} at 273 K and 1 bar. Besides, H-CuCo also demonstrates a much better gas separation performance of C_3H_6 to C_2H_4 than C-CuCo. The significantly enhanced performance toward gas adsorption and separation is attributed to the much higher specific surface area and unsaturated Cu sites in the framework of H-CuCo.

Results

Synthesis and structure characterization

Different from the common method using pure water as solvent to prepare C-CuCo with or without vacancies, H-CuCo with high crystallinity and open structure was synthesized through phase engineering strategy with a binary solvent system containing water and dimethylformamide (Fig. 1a). Supplementary Fig. 1 shows the detailed synthesis process of H-CuCo, neither high temperature/high pressure nor any other post-treatment is required (please see Supplementary information for details). Figure 1b shows the typical PXRD patterns of C-CuCo and H-CuCo, which indicate that the structure of H-CuCo is different from that of C-CuCo ($Fm\bar{3}m$, face-centered cubic (fcc) phase). The precise crystallographic structure of nano-sized H-CuCo remains elusive due to its small crystal size, which is unsuitable for conventional single-crystal X-ray diffraction that requires larger crystals. Although the structural refinement against high-quality PXRD data has been applied to probe host-guest interaction in the nano-sized crystalline porous materials with known crystallographic structures, solving the initial structure of unknown ones remains challenging due to peaks overlapping, structural disorder, and undesirable impurities[52–54].

The emerging 3D electron diffraction (ED) has been considered an effective method for ab initio structure determination of nanocrystals with unknown structure[55–58]. One of the specific methods called rotation electron diffraction (RED) has been utilized for solving initial structural models from a variety of functional crystalline materials[55,59]. Very recently, the updated technique named continuous RED (cRED) can collect hundreds of ED patterns within a short time (<5 min) and low electron dose rate[60,61]. The cRED data quality has been improved due to the 3D integration of electron intensity and the reduction of data collection time. Therefore, in this work, one cRED dataset was collected from the nano-sized H-CuCo for further structure determination. The hexagonal unit cell parameters can be deduced from this dataset. Moreover, reflection conditions were obtained from the 2D slices cut from the 3D reciprocal lattice (Fig. 1c–e) to be $h\text{-}hl$: $l = 2n$, which led to three possible space groups: $P6_3cm$ (No. 185), $P\bar{6}c2$ (No. 188), and $P6_3/mcm$ (No. 193). The cRED data (Supplementary Table 1) was further processed and intensities were extracted using X-ray Detector Software (XDS)[62]. Ab initio structure solution was performed with the highest space group (suggested by SHELXT) for the initial structure solution using direct methods implanted in SHELXT[63]. It shows that there are six Cu ions, four Co ions, and twenty-four cyanogen groups within a unit cell. Each Cu ion coordinates with four

cyanogen groups displaying a plane quadrilateral configuration, while each Co ion connects with six cyanogen groups showing an octahedral configuration. In this case, octahedra and quadrilateral are joined by sharing the cyanogen group alternatively, generating a 12-ring pore channel along the c-axis (only metal ions are considered), as shown Fig. 1a.

The chemical valences of Cu and Co ions in both H-CuCo and C-CuCo were investigated by XPS (Fig. 1f, g and Supplementary Fig. 2). For Co element, H-CuCo and C-CuCo show similar XPS patterns without satellite peaks, which correspond to Co^{III} for $Co\text{-}C\equiv N$ (Fig. 1f)[64,65]. But for the Co element in H-CuCo, there is a slight shift to lower binding energy compared with C-CuCo, which might be attributed to the different crystal structures. As shown in Fig. 1g, Cu^I and Cu^{II} coexist in both C-CuCo and H-CuCo. However, Cu^I signal is very strong in H-CuCo, with a ratio of 1.00/1.50 for Cu^I/Cu^{II}, much higher than that of C-CuCo (1.00/14.15). Besides, the Cu XPS peaks of H-CuCo also display a similar redshift in comparison with those of C-CuCo. Based on the above observations, the unit cell composition of a framework with the negative charges should be $[Cu^{+}_{2.4}Cu^{2+}_{3.6}Co^{3+}_4(CN)_{24}]^{2.4-}$. It is of interest to note that protonated dimethylamines (PDs) are countercations which are confirmed by ^1H nuclear magnetic resonance (NMR) (Supplementary Fig. 3) and thermogravimetric analysis (TGA) results (Supplementary Fig. 4). In the TGA profile, C-CuCo shows a sharp weight loss before ~170 °C, which should be associated with the removal of adsorbed water and zeolitic water. Then there is a second weight loss in the range of 170 to 290 °C, which should be ascribed to the elimination of coordinated water. The next sharp weight loss after ~290 °C is because of the decomposition of the material. In contrast, H-CuCo displays a different scenario in the first sharp weight loss, which happens before 120 °C and should be associated with the removal of adsorbed water and zeolitic water. Then a very flat step appears in the range from 120 to 260 °C, which indicates the limited impact of $M'(CN)_6$ vacancies that are associated with the coordinated water, suggesting almost no $M'(CN)_6$ vacancies in H-CuCo. And the flat step of 120 to 260 °C for H-CuCo should be attributed to the elimination of adsorbed dimethylformamide and PDs[66–68]. In order to further locate the positions of PDs, Rietveld refinement against PXRD data was used (Supplementary Fig. 5). Based on the initial structural model of CuCo-prism solved from cRED data, final Rietveld refinement results converged to weighted profile R factor (R_{wp}) = 1.86% and goodness of fit (GOF) = 2.18 (Supplementary Table 2). It shows that 2.4 PDs per unit cell are distributed in the 12-ring channels, balancing the negative charges from the framework. According to the cRED and simulation results, all the diffraction peaks of H-CuCo in Fig. 1b are confirmed, and the crystal indices and locations of characteristic peaks of H-CuCo and C-CuCo are shown in Supplementary Table 3.

Scanning electron microscope (SEM) and transmission electron microscope (TEM) images of H-CuCo show the hexagonal prism morphology, with a diameter and length of around 125 and 400 nm, respectively (Fig. 2a–c and Supplementary Fig. 6). For comparison, SEM (Supplementary Fig. 7) and TEM (Supplementary Fig. 8) images of common C-CuCo display the cube morphology, with an edge length of about 180 nm. Figure 2d shows the typical SAED pattern with sharp diffraction spots for H-CuCo, matching well with the [1$\bar{1}$0] zone axis of the hexagonal phase. The C_s-HRTEM image taken from [1$\bar{1}$0] zone axis exhibits clear and coherent lattice fringes with a spacing of 1.40 nm (Fig. 2e), which is assigned to the $(001)_h$ planes, and the corresponding fast Fourier transform (FFT) pattern further reveals the high crystallinity of H-CuCo (inset of Fig. 2e). Figure 2f shows the crystal model of H-CuCo along the [1$\bar{1}$0] zone axis. The high-angle annular dark-field scanning transmission electron microscope (HAADF-STEM) image and the corresponding elemental mappings demonstrate the uniform distribution of Cu, Co, C, and N in the entire structure of H-CuCo (Fig. 2g–k), consistent well with the energy-dispersive X-ray spectroscopy (EDS) analysis (Supplementary Figs. 9 and 10).
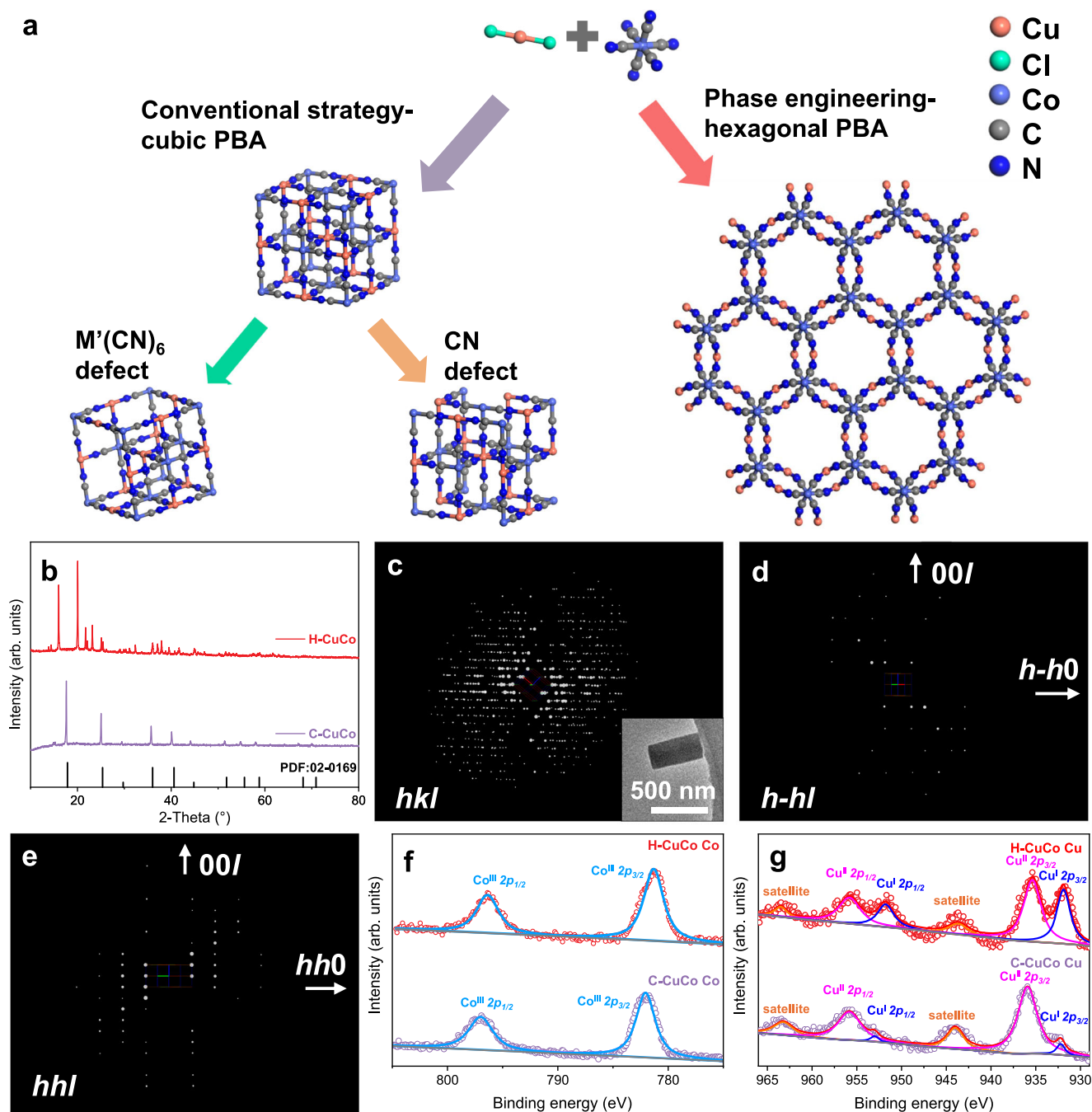
Fig. 1 | Synthesis and structure determination of CuCo PBAs. a The schematic illustrations for the synthesis of traditional cubic PBA with defect control and unconventional hexagonal PBA by phase engineering. All water molecules and countercations in crystal models are omitted for clarity. **b** PXRD patterns of H-CuCo and C-CuCo. **c–e** Reconstructed 3D reciprocal lattice of H-CuCo from cRED data (**c**) and two-dimensional slices of *h-hl* (**d**) and *hhl* (**e**). The reflection conditions are *h-hl*: *l=2n*. Inset of (**c**): TEM image of the corresponding H-CuCo for reconstructed 3D reciprocal lattice. **f**, **g** XPS spectra of Co (**f**) and Cu (**g**) for CuCo PBAs.

Gas uptake and separation performance

To confirm permanent porosity after solvent removal, Brunauer-Emmett-Teller (BET) analysis was performed by N_2 adsorption experiments at 77 K. Before the BET test, H-CuCo and C-CuCo were pre-treated at 100 °C under high vacuum for 12 h. The PXRD patterns before and after 48 h of treatments were collected (Supplementary Fig. 11, and Supplementary Tables 3 and 4), which are almost the same, suggesting the stable structure of both H-CuCo and C-CuCo. The typical BET profile of H-CuCo reveals a large specific surface area of 1273 $m^2\,g^{-1}$, which is almost three times that of common C-CuCo (443 $m^2\,g^{-1}$) (Fig. 3a). Compared with the traditional PBAs, the specific

surface area of H-CuCo is also much higher than the reported PBAs that usually feature a specific surface area of less than 900 $m^2\,g^{-1}$. Figure 3b shows that there are three types of pores in H-CuCo, whose half pore widths are 2.74, 4.30, and 6.16 Å, respectively, contributing to the pore volume of 0.800 $cm^3\,g^{-1}$, in contrast to only one major type of pores with half pore widths of 2.74 Å as well as the much smaller pore volume of 0.217 $cm^3\,g^{-1}$ for C-CuCo.

To reveal the gas adsorption performance, the sorption isotherms of single-component gases (such as CO_2, CH_4, C_2H_2, C_2H_4, C_2H_6, C_3H_6, and C_3H_8) were measured at 273 and 298 K for H-CuCo and C-CuCo, respectively (Fig. 3c–i, and Supplementary Table 5). In

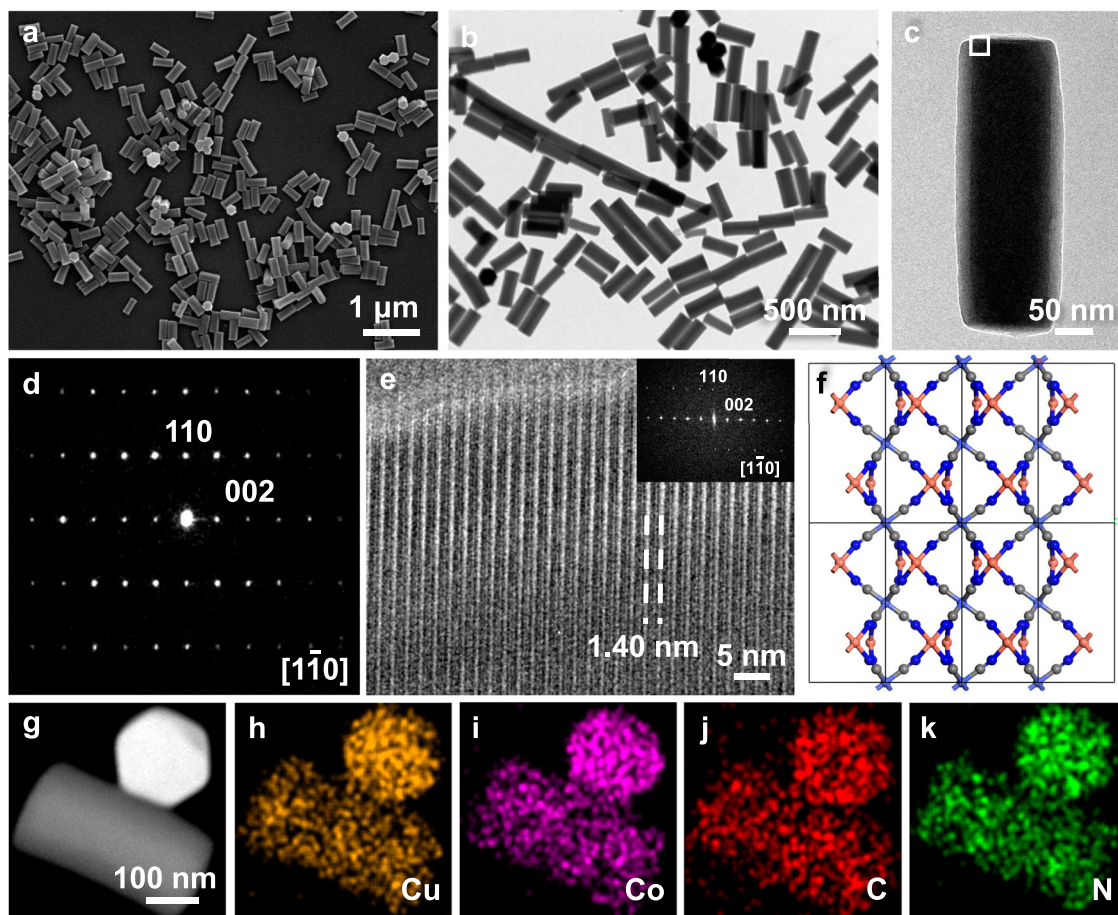**Fig. 2 | Structure characterization of H-CuCo. a–c** SEM image (**a**) and TEM images (**b, c**) of H-CuCo. **d** SAED pattern of H-CuCo along the [1$\bar{1}$0] zone axis. **e** C$_s$-HRTEM image taken from the white square-marked area in (**c**) and the corresponding FFT pattern as inset. **f** Crystal model of the lattice structure of H-CuCo along the [1$\bar{1}$0] zone axis. The orange, gray, and blue balls represent the Cu, C, and N atoms, respectively. **g–k** HAADF-STEM image (**g**) and the corresponding elemental mappings (**h–k**) of H-CuCo.

particular, it was observed that H-CuCo shows a high gravimetric CO$_2$ uptake capacity of 136.41 cm^3 g^{-1} (or 6.1 mmol g^{-1}) at 273 K and 1 bar, which indicates that H-CuCo captures 8.2 CO$_2$ molecules per unit cell. At 298 K and 1 bar, the CO$_2$ uptake capacity of H-CuCo still maintains a high level of 93.65 cm^3 g^{-1} (or 4.2 mmol g^{-1}). The aforementioned CO$_2$ uptake capacities of H-CuCo well surpass the values of 89.57 and 69.87 cm^3 g^{-1} (or 4.0 and 3.1 mmol g^{-1}) for C-CuCo at 273 and 298 K, 1 bar, respectively. Similarly, for CH$_4$, C$_2$H$_2$, C$_2$H$_4$, C$_2$H$_6$, C$_3$H$_6$, and C$_3$H$_8$, H-CuCo also exhibits much higher uptake capacities than those of C-CuCo under the same conditions, which further identifies that the hexagonal phase CuCo PBA possesses much better gas uptake capability than the conventional cubic phase counterpart. It is also worth mentioning that the CO$_2$ adsorption performance of H-CuCo is among the best compared with the previously reported porous materials (Supplementary Table 6). Moreover, as shown in Supplementary Fig. 12, the cycling measurements exhibit that the adsorption and desorption processes of H-CuCo are almost the same during the cycling, suggesting the high reversibility of H-CuCo for CO$_2$ capture (Supplementary Table 7). Additionally, the corresponding characterizations were made after the cycling test was conducted. As shown in Supplementary Fig. 13, the morphology of H-CuCo after the cycling test still shows the hexagonal prism shape. And based on the experimental and simulation results of H-CuCo, the XRD pattern of H-CuCo after cycling still demonstrates the unconventional hexagonal phase (Supplementary Fig. 14, and Supplementary Tables 3 and 8). These results indicate the good stability of H-CuCo for CO$_2$ capture.

Column breakthrough experiments of C$_3$H$_6$/C$_2$H$_4$ (50/50, v/v) were also conducted for H-CuCo and C-CuCo at 273 K. As shown in Supplementary Fig. 15, the C$_2$H$_4$ breakthrough occurs at 439 s/g on H-CuCo, similar to that on C-CuCo (412 s/g). However, the C$_3$H$_6$ is retained in the packed column of H-CuCo for 779 s/g, which is much longer than that of C-CuCo (670 s/g). The separation coefficient of C$_3$H$_6$ to C$_2$H$_4$ for H-CuCo is 6.82, which is over 2 times that of C-CuCo (3.35). Besides, H-CuCo also demonstrates greatly enhanced CO$_2$/CH$_4$ separation performance, in comparison with that of C-CuCo (Supplementary Fig. 16)[38]. These results suggest that phase engineering of PBAs provides a feasible and promising strategy for their applications in gas capture and separation.

Mechanism study

To uncover the mechanism of enhanced gas adsorption performance of H-CuCo, X-ray absorption fine structure (XAFS) analysis was performed to evaluate the local electronic and geometric structures of metal sites. Figure 4a shows the normalized Co K-edge X-ray absorption near edge structure (XANES) spectra of H-CuCo, C-CuCo, and K$_3$Co(CN)$_6$. The similar XANES patterns of Co further confirm that H-CuCo belongs to the PBA family. The well-overlapped pre-edge XANES curves of Co display that Co ions in H-CuCo, C-CuCo, and K$_3$Co(CN)$_6$ have almost the same valence and atomic environment of Co^{III} for Co-C≡N. In the corresponding Fourier transformed k^2-weighted extended X-ray absorption fine structure (EXAFS) spectra of Co K-edge (Fig. 4b), the peaks located at 1.47, 2.55, and 4.45 Å in R space are attributed to Co-C, Co-C≡N, and Co-C≡N-Cu scattering paths,
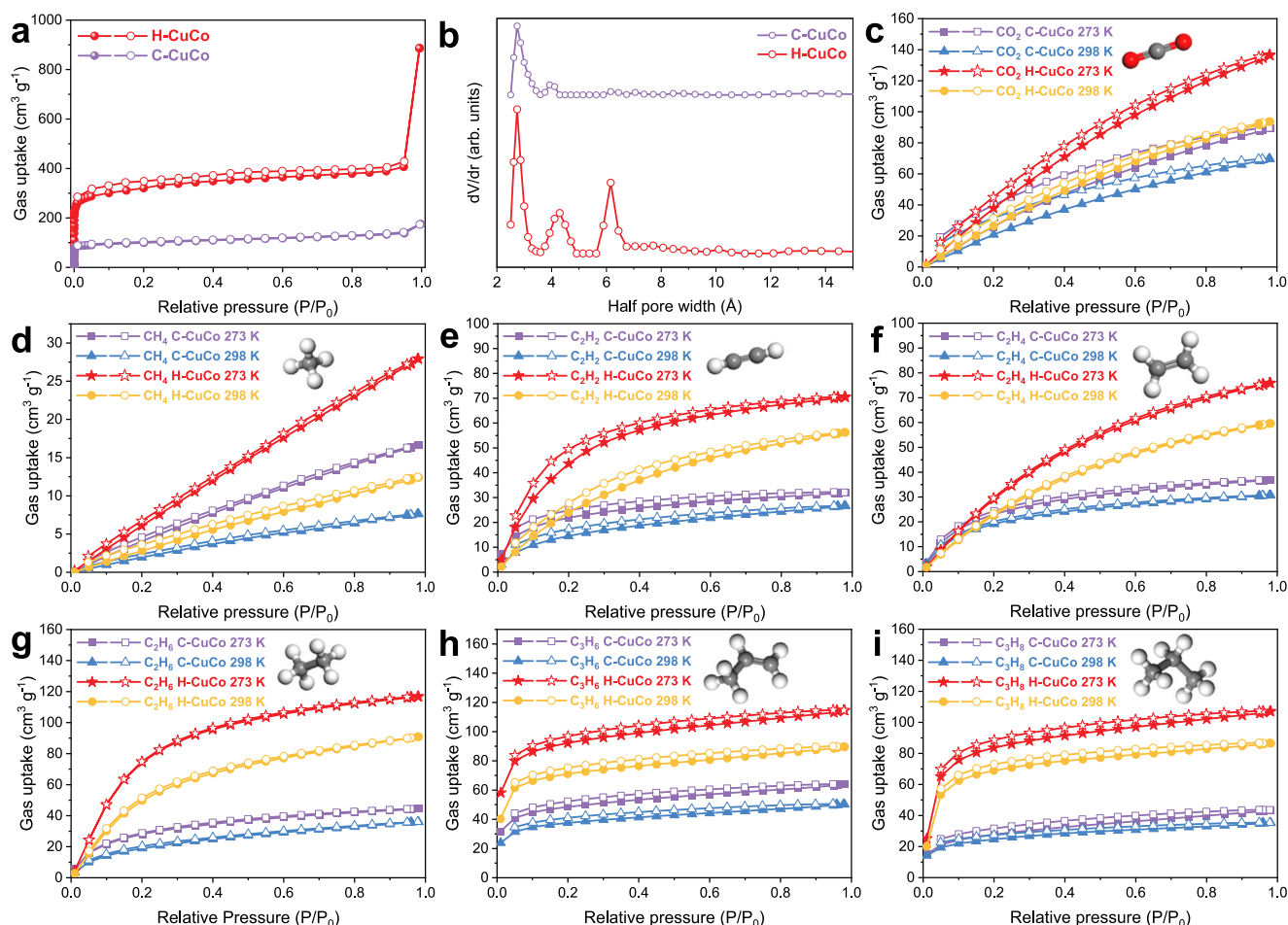
Fig. 3 | Gas sorption performance of H-CuCo and C-CuCo. a, b N_2 adsorption–desorption isotherms at 77 K (**a**) and pore size distributions (**b**) of H-CuCo and C-CuCo. **c–i** Gas adsorption–desorption isotherms of H-CuCo and C-CuCo for CO_2 (**c**), CH_4 (**d**), C_2H_2 (**e**), C_2H_4 (**f**), C_2H_6 (**g**), C_3H_6 (**h**), and C_3H_8 (**i**) at 1 bar and 273 or 298 K. The solid and open shapes represent the adsorption and desorption processes, respectively. The gray, white, and red balls represent the C, H, and O atoms, respectively.

respectively. It is worth noting that the above paths are nearly straight lines, resulting in a significant focusing effect, or in other words, linear multiple scattering. Consequently, we cannot describe these spectra using a purely single-scattering model. Based on the intensity of wavelet transforms (WTs) of Co K-edge EXAFS spectra (Supplementary Fig. 17), H-CuCo, C-CuCo, and $K_3Co(CN)_6$ show similar coordination numbers for Co-C and Co-C≡N, while the coordination number of Co-C≡N-Cu in H-CuCo is lower than that in C-CuCo.

The normalized Cu K-edge XAFS spectra of H-CuCo, C-CuCo, Cu_2O, CuO, and copper phthalocyanine (CuPc) were also acquired (Fig. 4c). The similar rising edge energies and white-line peak profiles of H-CuCo and C-CuCo confirm the PBA family feature of H-CuCo. There is a slight redshift for H-CuCo compared to C-CuCo, indicating a lower valence of Cu in H-CuCo. Referring to the shoulder peak of CuPc, the slightly higher shoulder peak intensity at around 8987 eV of H-CuCo suggests it possesses more Cu planar quadrilateral configurations than C-CuCo or a more significant Jahn–Teller effect. As shown in the Fourier transformed k^2-weighted EXAFS spectra of Cu (Fig. 4d), the peaks located at 1.56 and 2.60 Å in R space are assigned to Cu-N and Cu-N≡C scattering paths, respectively. The intensities of Cu-N for H-CuCo and C-CuCo are nearly the same, while the intensity of Cu-N≡C for H-CuCo is slightly lower than C-CuCo because of more Cu planar configurations. For peaks at 4.60 Å corresponding to the Cu-N≡C-Co scattering path, the peak intensity of H-CuCo is also obviously lower than C-CuCo, consistent with the observation based on the Fourier transformed k^2-weighted EXAFS spectra of Co. These features

have also been well confirmed by WTs of Cu K-edge EXAFS spectra (Fig. 4e-i).

After performing fitting of the EXAFS spectra of Co and Cu (Supplementary Figs. 18–21), detailed coordination parameters of H-CuCo and C-CuCo were obtained and listed in Supplementary Table 9. The results show that the coordination numbers of Co-C and Co-C≡N are the same for H-CuCo and C-CuCo, while the coordination numbers of Cu-N and Cu-N≡C in H-CuCo are much lower than those of C-CuCo, indicating the presence of unsaturated Cu sites that form the planar configuration, agreeing well with the former analysis. According to previous studies, the open metal sites can help elevate the uptake capacity and separation selectivity[8,38,69–73]. Therefore, it is considered that the superior gas uptake and separation performances of H-CuCo over C-CuCo not only arise from the much higher specific surface area but also benefit from the existence of unsaturated Cu sites with planar configurations and low valence states.

Extended synthesis

To expand the synthesis of hexagonal phase PBAs with open structures, we have introduced certain amounts of Fe, Co, Ni, and Zn precursors into the synthesis of H-CuCo, with the resultant products denoted as $Fe_{0.1}$-CuCo, $Fe_{0.2}$-CuCo, $Co_{0.1}$-CuCo, $Ni_{0.1}$-CuCo, and $Zn_{0.1}$-CuCo, respectively (please see detailed processes in the Supplementary information). As shown in Fig. 5, after doping different transition metal elements into H-CuCo while keeping all the other experimental conditions the same, both one-dimensional (Fig. 5a, b, e, f) and two-
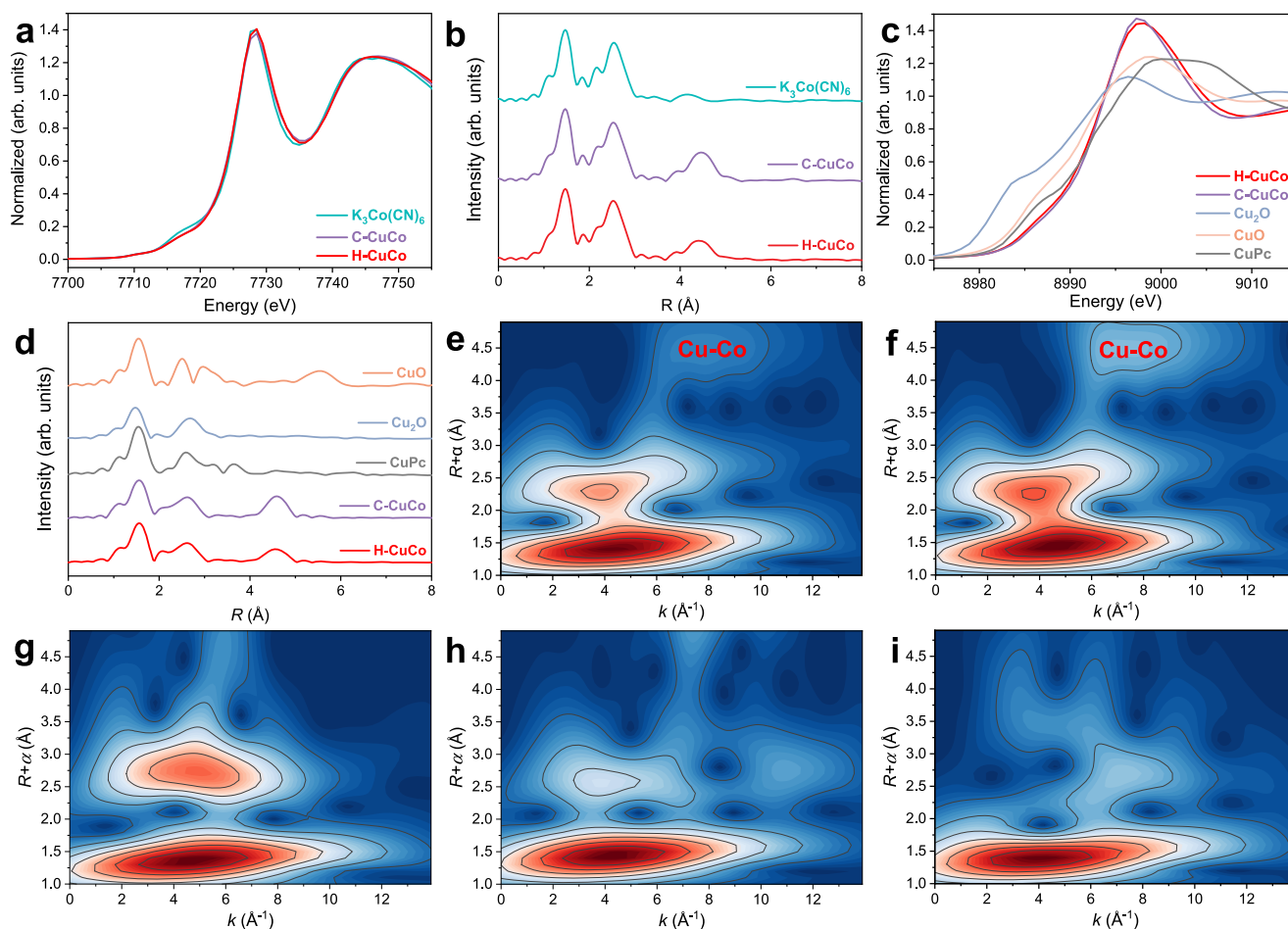
Fig. 4 | XAFS analysis of H-CuCo and C-CuCo. a–d Normalized Cu *K*-edge XANES spectra (**a**, **c**) and Fourier transformed k^2-weighted EXAFS spectra (**b**, **d**) of H-CuCo, C-CuCo and the reference samples. **e–i** The WTs of Cu *K*-edge EXAFS spectra for H-CuCo (**e**), C-CuCo (**f**), Cu_2O (**g**), CuO (**h**), and CuPc (**i**). The labeling of CuCo in Fig. 4e, f represents the Cu-N≡C-Co.

dimensional (Fig. 5i, j, m, n, q, r) PBA nanomaterials were obtained with high purity. The representative HAADF-STEM images and corresponding elemental mappings show the uniform distribution of individual transition metals within these as-prepared PBA nanostructures, indicating the successful introduction of dopant atoms into CuCo PBAs (Fig. 5c, g, k, o, s). Although the morphology has changed to some extent or dramatically, PXRD patterns of the obtained PBA nanocrystals reveal their unconventional hexagonal phase (Fig. 5d, h, l, p, t, and Supplementary Table 10).

To further investigate the effect of dopant atoms, XPS measurements were first performed for these 5 kinds of hexagonal CuCo-based PBAs (Supplementary Figs. 22–26). It was found that the ratio of Cu^I to Cu^{II} varies greatly along with the change of dopant atoms. Compared with H-CuCo, the content of Cu^I increases in $Fe_{0.1}$-CuCo, $Fe_{0.2}$-CuCo, $Ni_{0.1}$-CuCo, and $Zn_{0.1}$-CuCo, while it decreases in $Co_{0.1}$-CuCo. This observation suggests that the proportion of Cu^I sites in H-CuCo can be effectively modulated by introducing different dopant metal atoms. Specifically, the introduction of Ni, Fe, and Zn increases the content of Cu^I sites, while Co doping induces a reversed effect. Based on the XPS and inductively coupled plasma-mass spectrometry (ICP-MS) analysis of the ratio of Cu to Co (Supplementary Table 11), the chemical formulas of doped H-CuCo can be written as $[Fe^{3+}_{0.02}Cu^+_{1.32}Cu^{2+}_{0.44}Co^{3+}_1(CN)_6]^{0.74-}$, $[Fe^{3+}_{0.03}Cu^+_{1.25}Cu^{2+}_{0.42}Co^{3+}_1(CN)_6]^{0.82-}$, $[Co^{2+}_{0.16}Cu^+_{0.41}Cu^{2+}_{0.93}Co^{3+}_{0.84}(CN)_6]^{0.89-}$, $[Ni^{2+}_{0.06}Cu^+_{1.12}Cu^{2+}_{0.48}Co^{3+}_1(CN)_6]^{0.8-}$, and $[Zn^{2+}_{0.21}Cu^+_{1.09}Cu^{2+}_{0.38}Co^{3+}_1(CN)_6]^{0.73-}$ for $Fe_{0.1}$-CuCo, $Fe_{0.2}$-CuCo, $Co_{0.1}$-CuCo, $Ni_{0.1}$-CuCo, and $Zn_{0.1}$-CuCo, respectively. Moreover, the BET and single-component gas uptake measurements of doped CuCo PBAs

including hexagonal $Fe_{0.1}$-CuCo, $Fe_{0.2}$-CuCo, and $Co_{0.1}$-CuCo were also conducted to explore their gas adsorption properties (Supplementary Table 12 and Supplementary Figs. 27–34). Compared with $Co_{0.1}$-CuCo, $Fe_{0.1}$-CuCo exhibits higher specific surface area and much better gas uptake performance. Importantly, it was also observed that doping H-CuCo can significantly boost the gas uptake capacities of some hydrocarbon molecules like C_2H_2 and C_2H_4. However, it should be noted that too much doping of metal atoms in H-CuCo could decrease the specific surface area and lower the gas uptake performance as well.

Discussion

In summary, we have successfully developed a facile and general method to synthesize unconventional hexagonal open PBA structures via phase engineering. By combining 3D electron diffraction and other systematic characterizations, the hexagonal crystal structure of H-CuCo has been resolved, in which the Cu ion coordinated with four cyano groups via N possesses a planar quadrilateral configuration and the Co ion coordinated with six cyano groups via C owns an octahedral configuration, thereby forming a large 12-ring pore channel. In contrast with the traditional cubic structure CuCo PBA, this hexagonal phase CuCo PBA shows a larger specific surface area and also exhibits much better CO_2 adsorption performance, but also for CH_4, C_2H_2, C_2H_4, C_2H_6, C_3H_6, and C_3H_8. Simultaneously, H-CuCo delivers a superior separation performance of C_3H_6/C_2H_4 over the cubic counterpart and also holds a potential for CO_2/CH_4 separation. As probed by XPS and XAFS, large amounts of Cu^I and Cu-N≡C-Co with low
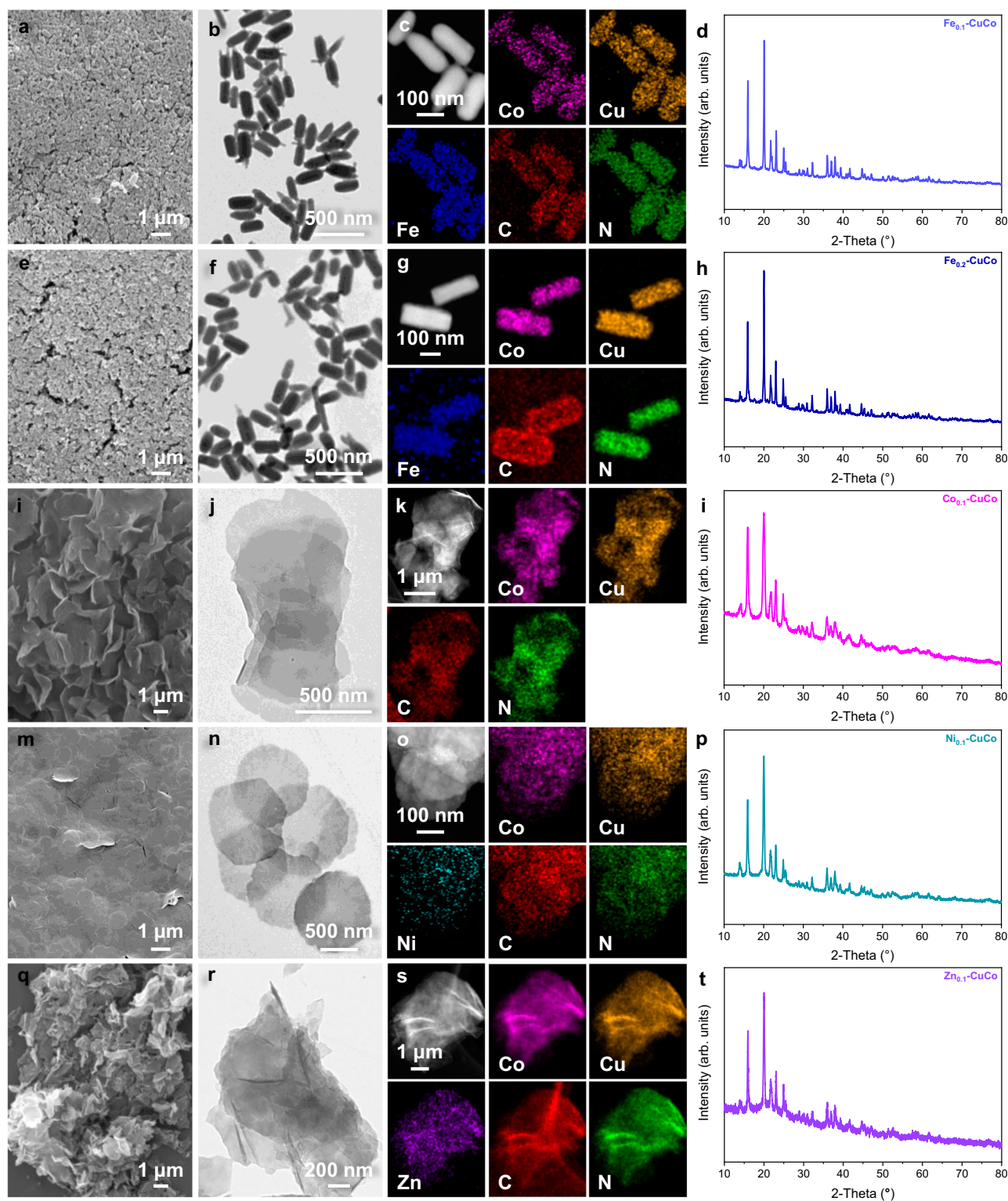
Fig. 5 | Extended synthesis and structure characterization of hexagonal PBAs. **a**, **e**, **i**, **m**, **q** SEM images, **b**, **f**, **j**, **n**, **r** TEM images, **c**, **g**, **k**, **o**, **s** HAADF-STEM images and the corresponding elemental mappings, and **d**, **h**, **l**, **p**, **t** PXRD patterns of hexagonal phase $Fe_{0.1}$-CuCo (**a–d**), $Fe_{0.2}$-CuCo (**e–h**), $Co_{0.1}$-CuCo (**i–l**), $Ni_{0.1}$-CuCo (**m–p**) and $Zn_{0.1}$-CuCo (**q–t**) PBAs.

coordination numbers exist in the unconventional H-CuCo, indicating the presence of unsaturated and open metal sites that can elevate the gas adsorption and separation performances. In addition, metal doping of H-CuCo has been developed to prepare various kinds of PBAs with hexagonal phases, which also feature rich unsaturated metal sites and tunable gas adsorption performance. It is believed that this study will inspire the rational design and preparation of high-performance PBAs and other porous materials as well as expand and promote their applications in various important fields beyond gas adsorption and separation, such as energy conversion and energy storage[74], catalysis[37,75], and cationic ion capture/recovery[76].

Methods

Materials

Potassium hexacyanocobaltate ($K_3Co(CN)_6$, 99%), (PVP, average M.W. 58,000), cobalt chloride hexahydrate ($CoCl_2 \cdot 6H_2O$, AR), copper chloride dihydrate ($CuCl_2 \cdot 2H_2O$, AR), nickel chloride hexahydrate ($NiCl_2 \cdot 6H_2O$, AR), zinc chloride ($ZnCl_2$, ACS Grade) and sodium citrate ($Na_3C_6H_5O_7$, AR, 99%) were purchased from Shanghai Aladdin. Ferric chloride hexahydrate ($FeCl_3 \cdot 6H_2O$, AR) was purchased from Dieckmann. Copper nitrate ($Cu(NO_3)_2$) was purchased from Macklin. Ethanol (ACS Grade, absolute) was purchased from Anaqua Global International Inc. Limited. Dimethylformamide (DMF, AR) was purchased from RCI Labscan. All the chemicals and materials were used as received without any further purification.

Synthesis of hexagonal phase CuCo Prussian blue analog prisms (H-CuCo)

For the synthesis of H-CuCo, a facile co-precipitation method was applied. Typically, 5 mL of de-ionized (DI) water containing 0.2 mmol of $CuCl_2 \cdot 2H_2O$ and 0.2 mmol of sodium citrate were added into the mixed solution of 5 mL of DI water and 25 mL of DMF containing 0.2 mmol of $K_3Co(CN)_6$ and 0.2 g of PVP. Then, the above solution was continuously stirred for 48 h in the water bath at 30 °C. After the reaction was completed, the precipitate was collected by centrifugation and rinsed with DI water and ethanol 3 times, respectively. Finally, the collected sample was dried at 80 °C for 12 h.

Synthesis of hexagonal phase Fe0.1-CuCo PBA

Typically, 5 mL of DI water containing 0.2 mmol of $CuCl_2 \cdot 2H_2O$, 0.02 mmol of $FeCl_3 \cdot 6H_2O$, and 0.2 mmol of sodium citrate were added into the mixed solution of 5 mL of DI water and 25 mL of DMF that containing 0.2 mmol of $K_3Co(CN)_6$ and 0.2 g of PVP. Then, the above solution was continuously stirred for 48 h in the water bath at 30 °C. After the reaction was completed, the precipitate was collected by centrifugation and rinsed with DI water and ethanol 3 times, respectively. Finally, the collected sample was dried in an oven at 80 °C for 12 h.

Synthesis of hexagonal phase Fe0.2-CuCo PBA

Typically, 5 mL of DI water containing 0.2 mmol of $CuCl_2 \cdot 2H_2O$, 0.04 mmol of $FeCl_3 \cdot 6H_2O$, and 0.2 mmol of sodium citrate were added into the mixed solution of 5 mL of DI water and 25 mL of DMF that containing 0.2 mmol of $K_3Co(CN)_6$ and 0.2 g of PVP. Then, the above solution was continuously stirred for 48 h in the water bath at 30 °C. After the reaction was completed, the precipitate was collected by centrifugation and rinsed with DI water and ethanol 3 times, respectively. Finally, the collected sample was dried in an oven at 80 °C for 12 h.

Synthesis of hexagonal phase Co0.1-CuCo PBA

Typically, 5 mL of DI water containing 0.2 mmol of $CuCl_2 \cdot 2H_2O$, 0.02 mmol of $CoCl_2 \cdot 6H_2O$, and 0.2 mmol of sodium citrate were added into the mixed solution of 5 mL of DI water, and 25 mL of DMF that containing 0.2 mmol of $K_3Co(CN)_6$ and 0.2 g of PVP. Then, the above solution was continuously stirred for 48 h in the water bath at 30 °C. After the reaction was completed, the precipitate was collected by centrifugation and rinsed with DI water and ethanol 3 times, respectively. Finally, the collected sample was dried in an oven at 80 °C for 12 h.

Synthesis of hexagonal phase Ni0.1-CuCo PBA

Typically, 5 mL of DI water containing 0.2 mmol of $CuCl_2 \cdot 2H_2O$, 0.02 mmol of $NiCl_2 \cdot 6H_2O$, and 0.2 mmol of sodium citrate were added into the mixed solution of 5 mL of DI water and 25 mL of DMF that containing 0.2 mmol of $K_3Co(CN)_6$ and 0.2 g of PVP. Then, the above

solution was continuously stirred for 48 h in the water bath at 30 °C. After the reaction was completed, the precipitate was collected by centrifugation and rinsed with DI water and ethanol 3 times, respectively. Finally, the collected sample was dried in an oven at 80 °C for 12 h.

Synthesis of hexagonal phase Zn0.1-CuCo PBA

Typically, 5 mL of DI water containing 0.2 mmol of $CuCl_2 \cdot 2H_2O$, 0.02 mmol of $ZnCl_2$, and 0.2 mmol of sodium citrate were added into the mixed solution of 5 mL DI water and 25 mL DMF containing 0.2 mmol of $K_3Co(CN)_6$ and 0.2 g of PVP. Then, the above solution was continuously stirred for 48 h in the water bath at 30 °C. After the reaction was completed, the precipitate was collected by centrifugation and rinsed with DI water and ethanol 3 times, respectively. Finally, the collected sample was dried in an oven at 80 °C for 12 h.

Synthesis of cubic phase CuCo PBA cubes (C-CuCo)

To prepare C-CuCo, 15 mL of DI water containing 0.145 g of $Cu(NO_3)_2$ and 0.75 mmol of sodium citrate were added into 15 mL of DI water containing 0.133 g of $K_3Co(CN)_6$, and then stirred for 12 h at room temperature. When the reaction finished, the precipitate was collected by centrifugation and rinsed with DI water and ethanol 3 times, respectively. Finally, the collected sample was dried in an oven at 80 °C for 12 h.

Characterizations

The as-synthesized samples were identified by power X-ray diffraction (XRD) (SmartLab, 40 kV) with K_α rays radiated from Cu. The scanning electron microscope (SEM) samples were prepared by dropping the suspension solution onto the silicon substrate and dried under ambient conditions. The SEM images were collected with a QUATTRO S SEM operated at 20 kV. The transmission electron microscope (TEM) images were acquired on JEOL JEM-2100F. The cRED data was collected on JEOL 2100plus equipped with an ASI camera at 200 kV. The high-resolution PXRD data for Rietveld refinement were collected on the STOE STADP diffractometer with a monochromatic Cu $K\alpha_1$ source ($\lambda = 1.5406$ Å) in the Debye−Scherrer geometry. The PXRD data were collected in the 0.2 mm capillary. The whole Rietveld refinement was performed with TOPAS academic suite V5.0. Thermogravimetry analysis (TGA) measurements were conducted on the PerkinElmer STA6000 analyzer from 30 to 650 °C at a rate of 10 °C min^{-1} under N_2 flow. The X-ray photoelectron spectroscopy (XPS) tests were performed using an ESCALAB-MKII spectrometer with an Al K_α X-ray source by using C 1 s (284.5 eV) as the reference. The X-ray absorption spectroscopy measurement was carried out in a transmission mode at the beamline X-ray absorption fine structure for catalysis (XAFCA) of Singapore Synchrotron Light Source operated at 700 MeV with a beam current of 200 mA[77]. The data was collected at room temperature. The data processing and fitting were conducted using the Athena and Artemis software packages[78]. The solution after saturated KCl exchange was analyzed by nuclear magnetic resonance (NMR 300 MHz, Bruker AVANCE III BBO Probe) spectroscopy. The ratio of Cu to Co in the obtained PBA samples was confirmed by the inductively coupled plasma optical emission spectrometry (ICP-OES, PerkinElmer, Optima 8000).

Single-component static adsorption

For the porosity analysis, nitrogen adsorption−desorption experiments were executed at 77 K on an Autosorb iQ2 adsorptometer, Quantachrome Instruments. The adsorption−desorption isotherms for CO_2, CH_4, and so on at 273 and 298 K were also recorded on the same instrument. Prior to the gas adsorption measurement, about 50 mg of the freshly prepared samples were activated under a high vacuum at 100 °C for 12 h. During the cycling tests, the samples were treated at 100 °C for 12 h after

each adsorption test, and then they were used for the next adsorption measurement.

Breakthrough experiments

The breakthrough experiments of C_3H_6/C_2H_4 were carried out with the Multi-constituent Adsorption Breakthrough equipment at 273 K. All experiments were conducted using a column with a 6 mm inner diameter and about 45 nm height. The weight of the packing sample is between 0.4 to 0.6 g. The column packed with samples was firstly activated at 373 K for 720 min and then purged with He flow (20 mL min^{-1}) at the target temperature. The mixed gas of C_3H_6 and C_2H_4 (50/50, v/v) flow was introduced at 5 mL min^{-1}. The outlet gas from the column was monitored by an online mass spectrometry. The breakthrough experiments of CO_2/CH_4 were conducted using a lab-scale fix-bed reactor at 298 K. In a typical experiment, the powder was activated at 373 K for 24 h. Then 100 mg of material was packed into a quartz column (5.8 mm (I.D.) × 150 mm) with silane-treated glass wool filling the void space. A helium flow (1 mL min^{-1}) was used to purge the adsorbent at 373 K for 5 h and then the system was cooled down to 298 K. The flow of helium was then turned off while the mixture of CO_2 and CH_4 (50/50, v/v) at a rate of 1 mL min^{-1} was allowed to flow into the column. The effluent from the column was monitored using an online mass spectrometer.

Data availability

The data that supports the findings of this study are included in the published article and its Supplementary Information. The crystallography information file (CIF) of typical samples is deposited at the Cambridge Crystallographic Data Centre (CCDC, http://www.ccdc.cam.ac.uk) under reference number 2324204 for H-CuCo. Source data are provided with this paper.

References

1. Nelson, J. *Progress in Inorganic Chemistry*. (Wiley, 1998).
2. Sharpe, A. G., *Chemistry of Cyano Complexes of the Transition Metals*. Academic Press (1976).
3. Keggin, J. F. & Miles, F. D. Structures and formulæ of the Prussian blues and related compounds. *Nature* **137**, 577–578 (1936).
4. Andonova, S. et al. Structure and properties of KNi–hexacyanoferrate Prussian blue analogues for efficient CO_2 capture: host–guest interaction chemistry and dynamics of CO_2 adsorption. *J. CO2 Util.* **50**, 101593 (2021).
5. Roque-Malherbe, R., Lugo, F. & Polanco, R. Synthesis, structural elucidation and carbon dioxide adsorption on Zn (II) hexacyanoferrate (II) Prussian blue analogue. *Appl. Surf. Sci.* **385**, 360–367 (2016).
6. Motkuri, R. K., Thallapally, P. K., McGrail, B. P. & Ghorishi, S. B. Dehydrated Prussian blues for CO_2 storage and separation applications. *CrystEngComm* **12**, 4003–4006 (2010).
7. Ojwang, D. O., Grins, J. & Svensson, G. The adsorption kinetics of CO_2 on copper hexacyanoferrate studied by thermogravimetric analysis. *Microporous Mesoporous Mater.* **272**, 70–78 (2018).
8. Karadas, F. et al. CO_2 adsorption studies on Prussian blue analogues. *Microporous Mesoporous Mater.* **162**, 91–97 (2012).
9. Roque-Malherbe, R., Carballo, E., Polanco, R., Lugo, F. & Lozano, C. Structure and adsorption properties of a porous cooper hexacyanoferrate polymorph. *J. Phys. Chem. Solids* **86**, 65–73 (2015).
10. Thallapally, P. K., Motkuri, R. K., Fernandez, C. A., McGrail, B. P. & Behrooz, G. S. Prussian blue analogues for CO_2 and SO_2 capture and separation applications. *Inorg. Chem.* **49**, 4909–4915 (2010).
11. Kaye, S. S. & Long, J. R. Hydrogen storage in the dehydrated Prussian blue analogues M$_3$[Co(CN)$_6$]$_2$ (M = Mn, Fe, Co, Ni, Cu, Zn). *J. Am. Chem. Soc.* **127**, 6506–6507 (2005).
12. Takahashi, A. et al. Historical pigment exhibiting ammonia gas capture beyond standard adsorbents with adsorption sites of two kinds. *J. Am. Chem. Soc.* **138**, 6376–6379 (2016).
13. Geng, S.-K. et al. Nickel ferrocyanide as a high-performance urea oxidation electrocatalyst. *Nat. Energy* **6**, 904–912 (2021).
14. Su, X. et al. Operando spectroscopic identification of active sites in NiFe Prussian blue analogues as electrocatalysts: activation of oxygen atoms for oxygen evolution reaction. *J. Am. Chem. Soc.* **140**, 11286–11292 (2018).
15. Yu, Z. Y. et al. Unconventional CN vacancies suppress iron-leaching in Prussian blue analogue pre-catalyst for boosted oxygen evolution catalysis. *Nat. Commun.* **10**, 2799 (2019).
16. Song, N., Ren, S., Zhang, Y., Wang, C. & Lu, X. Confinement of Prussian blue analogs boxes inside conducting polymer nanotubes enables significantly enhanced catalytic performance for water treatment. *Adv. Funct. Mater.* **32**, 2204751 (2022).
17. Singh, B. et al. Deciphering ligand controlled structural evolution of prussian blue analogues and their electrochemical activation during alkaline water oxidation. *Angew. Chem. Int. Ed.* **61**, e202211585 (2022).
18. Shi, J. et al. Prussian blue analogs photocatalyst promote the evolution of value-added platform compounds via Co-CN-Zn covalent bonds. *EcoMat* **6**, e12441 (2024).
19. Peng, J. et al. A dual-insertion type sodium-ion full cell based on high-quality ternary-metal Prussian blue analogs. *Adv. Energy Mater.* **8**, 1702856 (2018).
20. Peng, J. et al. Defect-free-induced Na$^+$ disordering in electrode materials. *Energy Environ. Sci.* **14**, 3130–3140 (2021).
21. Song, J. et al. Removal of interstitial H_2O in hexacyanometallates for a superior cathode of a sodium-ion battery. *J. Am. Chem. Soc.* **137**, 2658–2664 (2015).
22. Yin, J. et al. Controlled synthesis of 2D Prussian blue analog nanosheets with low coordinated water content for high-performance lithium storage. *Small Methods* **6**, e2201107 (2022).
23. Zhou, Q., Liu, H. K., Dou, S. X. & Chong, S. Defect-free Prussian blue analogue as zero-strain cathode material for high-energy-density potassium-ion batteries. *ACS Nano* **18**, 7287–7297 (2024).
24. Zhao, X. et al. Four-electron redox reaction in Prussian blue analogue cathode material for high-performance sodium-ion batteries. *ACS Energy Lett.* **9**, 2748–2757 (2024).
25. Shou, P. et al. Zn^{2+} doped ultrasmall Prussian blue nanotheranostic agent for breast cancer photothermal therapy under MR imaging guidance. *Adv. Health. Mater.* **9**, e1900948 (2020).
26. Wu, W. et al. Copper-enriched Prussian blue nanomedicine for in situ disulfiram toxification and photothermal antitumor amplification. *Adv. Mater.* **32**, e2000542 (2020).
27. Wang, L.-C. et al. Prussian blue analog with separated active sites to catalyze water driven enhanced catalytic treatments. *Nat. Commun.* **14**, 4709 (2023).
28. Cai, X. et al. A Prussian blue-based core–shell hollow-structured mesoporous nanoparticle as a smart theranostic agent with ultrahigh pH-responsive longitudinal relaxivity. *Adv. Mater.* **27**, 6382–6389 (2015).
29. Shokouhimehr, M. et al. Dual purpose Prussian blue nanoparticles for cellular imaging and drug delivery: a new generation of T$_1$-weighted MRI contrast and small molecule delivery agents. *J. Mater. Chem.* **20**, 5251–5259 (2010).
30. Busquets, M. A. & Estelrich, J. Prussian blue nanoparticles: synthesis, surface modification, and biomedical applications. *Drug Discov. Today* **25**, 1431–1443 (2020).
31. Kong, B., Selomulya, C., Zheng, G. & Zhao, D. New faces of porous Prussian blue: interfacial assembly of integrated heterostructures for sensing applications. *Chem. Soc. Rev.* **44**, 7997–8018 (2015).

32. Imani, S. et al. A wearable chemical-electrophysiological hybrid biosensing system for real-time health and fitness monitoring. *Nat. Commun.* **7**, 11650 (2016).

33. Lin, Y. et al. Porous enzymatic membrane for nanotextured glucose sweat sensors with high stability toward reliable noninvasive health monitoring. *Adv. Funct. Mater.* **29**, 1902521 (2019).

34. Ma, X. et al. Prussian blue nanozyme as a pyroptosis inhibitor alleviates neurodegeneration. *Adv. Mater.* **34**, e2106723 (2022).

35. Feng, L. S. et al. Enhancement of nanozyme permeation by endovascular interventional treatment to prevent vascular restenosis via macrophage polarization modulation. *Adv. Funct. Mater.* **30**, 2006581 (2020).

36. Simonov, A. et al. Hidden diversity of vacancy networks in Prussian blue analogues. *Nature* **578**, 256–260 (2020).

37. Peng, J. et al. Cold plasma-activated Cu-Co catalysts with CN vacancies for enhancing CO_2 electroreduction to low-carbon alcohol. *J. Energy Chem.* **85**, 108–115 (2023).

38. Chand Pal, S., Krishna, R. & Das, M. C. Highly scalable acid-base resistant Cu-Prussian blue metal-organic framework for C_2H_2/C_2H_4, biogas, and flue gas separations. *Chem. Eng. J.* **460**, 141795 (2023).

39. Kaye, S. S. & Long, J. R. Hydrogen adsorption in dehydrated variants of the cyano-bridged framework compounds $A_2Zn_3[Fe(CN)_6]_2 \cdot xH_2O$ (A = H, Li, Na, K, Rb). *Chem. Commun.* **21**, 4486–4488 (2007).

40. Kaye, S. S. & Long, J. R. The role of vacancies in the hydrogen storage properties of Prussian blue analogues. *Catal. Today* **120**, 311–316 (2007).

41. Zhang, W. et al. Core-shell Prussian blue analogs with compositional heterogeneity and open cages for oxygen evolution reaction. *Adv. Sci.* **6**, 1801901 (2019).

42. Zhang, W. et al. Synthesis of monocrystalline nanoframes of Prussian blue analogues by controlled preferential etching. *Angew. Chem. Int. Ed.* **55**, 8228–8234 (2016).

43. Boström, H. L. B. et al. Probing the influence of defects, hydration, and composition on Prussian blue analogues with pressure. *J. Am. Chem. Soc.* **143**, 3544–3554 (2021).

44. Escax, V. et al. Photoinduced ferrimagnetic systems in Prussian blue analogues $CI_xCo_4[Fe(CN)_6]_y$ (CI = Alkali Cation). 3. Control of the photo- and thermally induced electron transfer by the $[Fe(CN)_6]$ vacancies in cesium derivatives. *J. Am. Chem. Soc.* **123**, 12536–12543 (2001).

45. Kang, Y. et al. $[Fe(CN)_6]$ vacancy-boosting oxygen evolution activity of Co-based Prussian blue analogues for hybrid sodium-air battery. *Mater. Today. Energy* **20**, 100572 (2021).

46. Liu, J. et al. Vacancies-regulated Prussian blue analogues through precipitation conversion for cathodes in sodium-ion batteries with energy densities over 500 Wh/kg. *Angew. Chem. Int. Ed.* **63**, e202400214 (2024).

47. Lai, C. et al. 3D spatial combination of CN vacancy-mediated NiFe-PBA with N-doped carbon nanofibers network toward free-standing bifunctional electrode for Zn-air batteries. *Adv. Sci.* **9**, e2105925 (2022).

48. Deng, W. et al. C≡N vacancy engineering of Prussian blue analogs for the advanced oxygen evolution reaction. *J. Environ. Chem. Eng.* **11**, 109407 (2023).

49. Xie, B. et al. Recent progress of Prussian blue analogues as cathode materials for nonaqueous sodium-ion batteries. *Coord. Chem. Rev.* **460**, 214478 (2022).

50. Zakaria, M. B. & Chikyow, T. Recent advances in Prussian blue and Prussian blue analogues: synthesis and thermal treatments. *Coord. Chem. Rev.* **352**, 328–345 (2017).

51. Li, W. J. et al. Chemical properties, structural properties, and energy storage applications of Prussian blue analogues. *Small* **15**, e1900470 (2019).

52. Guo, P. et al. A zeolite family with expanding structural complexity and embedded isoreticular structures. *Nature* **524**, 74–78 (2015).

53. Liu, X. et al. The complex crystal structure and abundant local defects of zeolite EMM-17 unraveled by combined electron crystallography and microscopy. *Angew. Chem. Int. Ed.* **60**, 24227–24233 (2021).

54. Yun, Y., Zou, X., Hovmoller, S. & Wan, W. Three-dimensional electron diffraction as a complementary technique to powder X-ray diffraction for phase identification and structure solution of powders. *IUCrJ* **2**, 267–282 (2015).

55. Zhang, D., Oleynikov, P., Hovmöller, S. & Zou, X. Collecting 3D electron diffraction data by the rotation method. *Z. Kristallogr.* **225**, 94–102 (2010).

56. Shi, D., Nannenga, B. L., Iadanza, M. G. & Gonen, T. Three-dimensional electron crystallography of protein microcrystals. *eLlife* **2**, e01345 (2013).

57. Nannenga, B. L., Shi, D., Leslie, A. G. W. & Gonen, T. High-resolution structure determination by continuous-rotation data collection in MicroED. *Nat. Methods* **11**, 927–930 (2014).

58. Kolb, U., Gorelik, T., Kubel, C., Otten, M. T. & Hubert, D. Towards automated diffraction tomography: part I-data acquisition. *Ultramicroscopy* **107**, 507–513 (2007).

59. Wan, W., Sun, J., Su, J., Hovmoller, S. & Zou, X. Three-dimensional rotation electron diffraction: software RED for automated data collection and data processing. *J. Appl. Crystallogr.* **46**, 1863–1873 (2013).

60. Cichocka, M. O., Ångström, J., Wang, B., Zou, X. & Smeets, S. High-throughput continuous rotation electron diffraction data acquisition via software automation. *J. Appl. Crystallogr.* **51**, 1652–1661 (2018).

61. Wang, Y. et al. Elucidation of the elusive structure and formula of the active pharmaceutical ingredient bismuth subgallate by continuous rotation electron diffraction. *Chem. Commun.* **53**, 7018–7021 (2017).

62. Kabsch, W. Xds. *Acta Crystallogr. D.* **66**, 125–132 (2010).

63. Sheldrick, G. M. SHELXT - integrated space-group and crystal-structure determination. *Acta Crystallogr. A* **71**, 3–8 (2015).

64. Oku, M. & Hirokawa, K. X-ray photoelectron spectroscopy of Co_3O_4, Fe_3O_4, Mn_3O_4, and related compounds. *J. Electron Spectrosc. Relat. Phenom.* **8**, 475–481 (1976).

65. Oku, M., Hirokawa, K. & Ikeda, S. Photoelectron spectral intensities of some first transition series elements in metal cyanides containing inequivalent atoms. *J. Electron Spectrosc. Relat. Phenom.* **6**, 451–458 (1975).

66. Grebenyuk, D. et al. Tuning the cerium-based metal–organic framework formation by template effect and precursor selection. *ACS Omega* **8**, 48394–48404 (2023).

67. Szufla, M., Navarro, J. A. R., Góra-Marek, K. & Matoga, D. Effect of missing-linker defects and ion exchange on stability and proton conduction of a sulfonated layered Zr-MOF. *ACS Appl. Mater. Interfaces* **15**, 28184–28192 (2023).

68. Zhou, Y. et al. Tuning pore polarization to boost ethane/ethylene separation performance in hydrogen-bonded organic frameworks. *Angew. Chem. Int. Ed.* **62**, e202305041 (2023).

69. Xie, Y., Lin, R. B. & Chen, B. Old materials for new functions: recent progress on metal cyanide based porous materials. *Adv. Sci.* **9**, e2104234 (2022).

70. Bloch, E. D. et al. Hydrocarbon separations in a metal-organic framework with open iron (II) coordination sites. *Science* **335**, 1606–1610 (2012).

71. Yuan, W. et al. Building stable pillar-layered metal–organic frameworks: introduction of unsaturated bonds for enhanced efficiency in C_2H_2/CO_2 separation. *ACS Mater. Lett.* **6**, 3925–3931 (2024).

72. Niu, Z. et al. A MOF-based ultra-strong acetylene nano-trap for highly efficient C_2H_2/CO_2 separation. *Angew. Chem. Int. Ed.* **60**, 5283–5288 (2021).

73. Zhang, Z. et al. Efficient trapping of trace acetylene from ethylene in an ultramicroporous metal–organic framework: synergistic effect of high-density open metal and electronegative sites. *Angew. Chem. Int. Ed.* **59**, 18927–18932 (2020).

74. Ma, L. et al. Electrocatalytic selenium redox reaction for high-mass-loading zinc-selenium batteries with improved kinetics and selenium utilization. *Adv. Energy Mater.* **12**, 2201322 (2022).

75. Meng, X. et al. Light-driven CO_2 reduction over Prussian blue analogues as heterogeneous catalysts. *ACS Catal.* **12**, 89–100 (2022).

76. Han, W. et al. Highly selective adsorption and lattice process of cesium by cubic cyanide-based functional materials. *Environ. Res* **214**, 114085 (2022).

77. Du, Y. et al. XAFCA: a new XAFS beamline for catalysis research. *J. Synchrotron Radiat.* **22**, 839–843 (2015).

78. Newville, M. IFEFFIT: interactive XAFS analysis and FEFF fitting. *J. Synchrotron Radiat.* **8**, 322–324 (2001).

Acknowledgements

Author contributions

J.Y. designed the experiments, synthesized the materials, performed most of the initial tests, and analyzed the data. J.W. and P.G. conducted the Rietveld refinements, and cRED test and solved the structure. M.S. and B.H. conducted the theoretical calculations. Y.-J.Y. and Y.Y. conducted the BET test and single gas sorption measurements. J.L. and D.Z. conducted the C_s-HRTEM characterization. L.W. and Z.Z. conducted the PXRD measurements. X.D. and Y.H. conducted the gas breakthrough test. H.B. and W.N. conducted the XPS tests. S.X. performed the XAFS measurement and fitting. J.Y. and C.Y. analyzed the XAFS data. J.G., B.C., X.Z., L.Z., Z.L., Z.H., Q.L., X.M., Y.M., J.Z., P.L., and Y.W. participated in partial experiments. J.Y., J.W., Y.Y., B.H., P.G., and Z.F. organized the work and helped with the draft of the manuscript. The project was proposed, administrated, and guided by Z.F. All the authors discussed the results and revised the final manuscript.

Competing interests

The authors declare no competing interests.

Additional information

Supplementary information The online version contains supplementary material available at https://doi.org/10.1038/s41467-024-55775-w.

Correspondence and requests for materials should be addressed to Ye Yuan, Bolong Huang, Peng Guo or Zhanxi Fan.

Peer review information *Nature Communications* thanks Mohamed Hegazy and the other, anonymous, reviewer(s) for their contribution to the peer review of this work. A peer review file is available.

Reprints and permissions information is available at http://www.nature.com/reprints

Publisher's note Springer Nature remains neutral with regard to jurisdictional claims in published maps and institutional affiliations.

¹Department of Chemistry, City University of Hong Kong, Kowloon, Hong Kong, China. ²Hong Kong Branch of National Precious Metals Material Engineering Research Center (NPMM), City University of Hong Kong, Kowloon, Hong Kong, China. ³National Engineering Research Center of Lower-Carbon Catalysis Technology, Dalian Institute of Chemical Physics, Chinese Academy of Sciences, Dalian 116023, Liaoning, China University of Chinese Academy of Sciences, Beijing, China. ⁴College of Environmental Science and Engineering, Dalian Maritime University, Dalian, China. ⁵Department of Applied Biology and Chemical Technology, The Hong Kong Polytechnic University, Kowloon, Hong Kong, China. ⁶Key Laboratory of Polyoxometalate and Reticular Material Chemistry of Ministry of Education, Faculty of Chemistry, Northeast Normal University, Changchun, China. ⁷Multi-scale Porous Materials Center, Institute of Advanced Interdisciplinary Studies, & School of Chemistry and Chemical Engineering, Chongqing University, Chongqing, China. ⁸Advanced Membranes and Porous Materials Center, Physical Sciences and Engineering Division, King Abdullah University of Science and Technology, Thuwal, Saudi Arabia. ⁹Catalyst Center of Excellence (CCoE), Research and Development Center, Saudi Aramco, Dhahran, Saudi Arabia. ¹⁰Department of Power Engineering, North China Electric Power University, Baoding, China. ¹¹State Key Laboratory of Electroanalytical Chemistry, Changchun Institute of Applied Chemistry, Chinese Academy of Sciences, Changchun, China. ¹²Center for Electron Microscopy, South China University of Technology, Guangzhou, China. ¹³Institute of Sustainability for Chemicals, Energy and Environment (ISCE2), Agency for Science, Technology and Research (A*STAR), 1 Pesek Road, Jurong Island, Singapore, Republic of Singapore. ¹⁴University of Chinese Academy of Sciences, Beijing, China. ¹⁵Hong Kong Institute for Clean Energy, City University of Hong Kong, Kowloon, Hong Kong, China. ¹⁶City University of Hong Kong Shenzhen Research Institute, Shenzhen, China. ¹⁷These authors contributed equally: Jinwen Yin, Jing Wang, Mingzi Sun, Yajie Yang, Jia Lyu. ✉e-mail: yuany101@nenu.edu.cn; bhuang@polyu.edu.hk; pguo@dicp.ac.cn; zhanxi.fan@cityu.edu.hk